Abstracting topology, shape and size from heterogenous microstructure.

Amal Aboulhassan[b], Markus Hadwiger[b], Olga Wodo[a,*]

[a] *Department of Materials Design and Innovation, University at Buffalo, Buffalo, New York, USA*
[b] *Visual Computing Center, King Abdullah University of Science and Technology, Thuwal, Saudi Arabia*

Abstract

Materials with tailored microstructures are an emerging class of materials with applications to battery electrodes, organic electronics, and biosensors. Tailoring microstructural features that control properties of these materials depends on the ability to first identify the salient features governing properties and next to alter the microstructure accordingly. Choosing robust microstructure representation is pivotal towards completing both steps. In this paper, we focus on the first step and present the methodology for abstracting and quantifying a hierarchical set of microstructural features covering topology, shape and size aspects of the microstructure. Finally, we leverage this methodology to determine the coarsening rates of microstructure expressed in terms of four different microstructural features.

Keywords: feature extraction, microstructural descriptor, organic solar cells, heterogenous microstructure, computational geometry, clustering

1. Introduction

Quantifying structural features from microstructural samples is a fundamental step for establishing reliable structure-property relationships in materials (SPR). Establishing SPR provides quantitative means to understanding the behavior of materials subjected to various stimuli, but it is rarely a trivial task for several reasons [1, 2, 3]. First of all, the structure of materials has a wide spectrum of features ranging from atomistic to microstructural that may involve chemical, compositional, geometrical or topological characteristics. Although each feature, or combination of features, may potentially govern the materials properties of interest, it is reasonable to assume that only some structure aspects control the given class of properties. With such an assumption, the goal of quantitative SPR is to identify salient features of the microstructure that reliably explains most of the variability of the behavior of materials under consideration. The distilled key features become the basis for the predictive modeling, exploration, optimization, and design of materials with desired properties.

The textbook example of SPR relations is the Hall-Petch scaling law [4]. It explains the strength of the materials through the average grain size of the microstructure. This law has

*Tel.:+1 716-645-1377. E-mail address: olgawodo@buffalo.edu

been harnessed to explain the properties for a wide spectrum of materials [5]. The average grain size, or in the more general case the characteristic length scale, is typically the first choice for the salient features. Nevertheless, the geometrical [6] and topological aspects [7] are more and more often discussed in the context of structural features governing properties of materials. For example, Mangipud et al. [7] showed that the prefactor in scaling law of stiffness and strength of nanoporous materials scales linearly with the genus of topology. This is an important example of SPR as it demonstrates that a more general SPR can be derived if the expanded set of structural features is available.

The above example belongs to the hypothesis-driven protocol for deriving SPRs, where carefully designed experiments generate samples spanning the preferably wide range of structural features and properties. Physical laws are used to interpret the results and propose scaling laws. Recently, another class of SPR has emerged that is based on machine learning to generate the model from large and diverse sample sets. In this approach, each sample is annotated with a suite of descriptors that may govern measured properties. Statistical methods are subsequently used to discover the SPRs. These SPRs are high predictive capabilities but do not necessarily provide a physical explanation. Finally, visualization methods are also developed to facilitate the visual inspection of the microstructural features and their link with the properties [8, 9, 10]. All these approaches have their strength and weaknesses, but they both rely on the structural characterization. Especially the second one heavily depends on the exhaustive structural characterization.

In this paper, we address the need for comprehensive microstructure characterization with focus on hierarchical feature extraction. We describe the methodology to simultaneously extract topological features, shape and size characteristics from heterogenous microstructural samples. We apply the skeletonization algorithm to extract the topology of the microstructure. Next, we segment the backbone to demarcate mesoscale patches. Finally, we characterize each patch with local features, e.g., curvature, to infer shape and size. This is a unique aspect of morphology quantification, as it allows extraction of the local features rather than volume averaged quantities. We apply this methodology to quantify the morphology evolution of spinodal decomposition and derive the corresponding scaling laws for selected features. Although Park et al. demonstrated the evolution of local principal curvatures for spinodal decomposition. [11], the authors derived the semi-analytical approach to rate laws for the mean curvature. In this paper, we focus on the morphological segments and patches providing more comprehensive insight into the morphological features.

2. Hierarchical feature extraction from microstructure sets

We propose the hierarchical feature extraction that consists of three steps. In the first step, we extract the topology of the microstructure by determining the skeleton or backbone of the microstructure (see Fig. 1). Next, using the skeleton as a topological abbreviation of the microstructure, we partition the microstructure into patches. In particular, we generate patches along the skeleton (see Fig. 3(a)) with patch size dictated by the local resolution of the microstructural features. Finally, for each patch, we further characterize its shape by calculating the curvature distribution (see Fig. 3(d)).

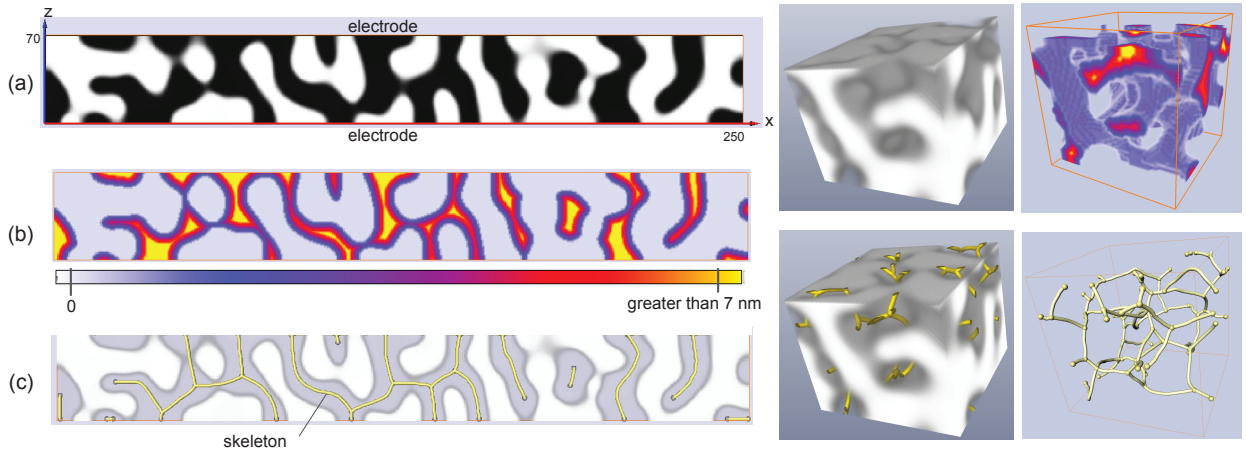

Figure 1: The elements involved in extracting the skeleton: the left column illustrates the steps for 2D while the right column illustrates them for 3D. Panel (a) shows the original morphology. The black regions represent one phase, white regions represent the second phase and the gray region in between represents the interface. The blue axis represents the z-direction along film thickness while the red axis represents the x-direction. The anode corresponds to the line parallel to the x-direction at z=70 while the cathode is the line at z=0. Panel (b) shows the distance field computed from the given morphology. The color code reflects the distance from each voxel to the nearest interface. The figure shows a color map which assigns yellow to all distances bigger than 7 pixels. Panel (c) shows the skeleton computed from the distance field overlaid on a transparent slice of the given morphology. The skeleton represents the medial axis inside the black phase.

2.1. Microstructure representation

Microstructure is typically imaged via microscopy [12, 13] or predicted by numerical simulation [14, 15]. Depending on the specifics of the techniques used, the level of information extracted from the sample varies. For example, atom probe tomography [16] or molecular dynamic simulations [15] extract the information about position of individual atoms, while optical microscope [12], tomography or continuum simulations [14, 3] stores information in the voxel-based format. For this work, we assume that microstructure is stored as an array of voxels Z, where each voxel encodes the local phase. For two-phase microstructure, a phase is given as discrete variable $\{0, 1\}$, where 0 represents one phase (marked black in figures) while 1 represents the second phase (marked white in figures).

Extracting topology of heterogenous microstructure

In the first step, we extract the microstructural backbone using skeletonization algorithm [17]. Skeletonization is a classical algorithm in computational geometry that extracts the medial axis from 3D volumes. In general, the medial axis is the subset of points (from input 3D volume) having more than one closest point on the object's boundary. For example, Figure 1 (a and c) depict the two-phase input morphology and the corresponding skeleton determined for one phase (black phase for 2D microstructure and semi-transparent grey for 3D microstructure, respectively). Note that determined skeleton constitutes the medial axis for the black domains where the white/black interface is the object boundary. The analogous skeleton can be determined for the opposite phase.

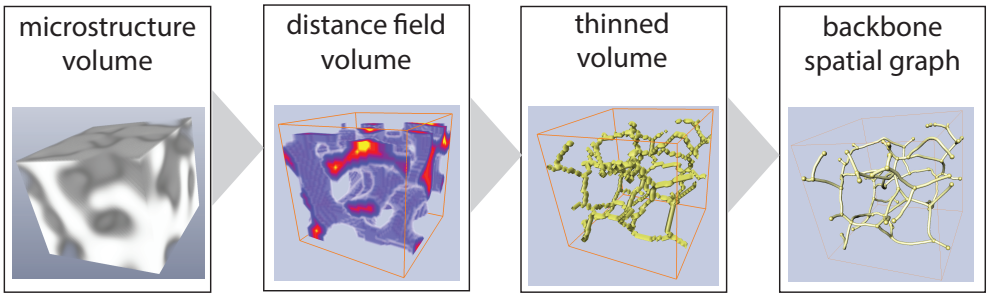

Figure 2: The steps of extracting the skeleton: distance field calculation to the interface, the thinning algorithm resulting in the subset of voxels, and spatial graph construction.

In general, different approaches for performing skeletonization exist (distance transform [18], Voronoi based [19], thinning [20, 17]). In this paper, we leverage the thinning algorithm proposed by Pudney [17]. Details of the algorithm are given in the original paper [17], and here we only provide the outline of basic steps to introduce basic terms required to describe our method.

The algorithm involves three main steps (Figure 2): (i) calculating distance map to the boundary, (ii) volume thinning, and (iii) spatial graph construction. The distance map generates a distance field (in our case, it is the set of shortest distances from each black voxel to the interface (as shown in Fig. 1 b)). Instead of using the actual Euclidean distance metric, the algorithm uses the chamfer distance transform, that determines the order of the voxel from the interface. The transform is defined by :

$$d(p) = min\{d(q) + D(p,q)\}, p \in F, q \in N_{26}(p), 0 \; otherwise \tag{1}$$

where $N_{26}(p)$ is the set of 26 neighbor voxels of p ($3 \times 3 \times 3$).

The order of voxels, $d(p)$, is a crucial element of the second step of the algorithm when voxels are successively deleted based on the order in the distance map. At the end of this step, the medial axis is determined as a subset of the input set. Formally, the thinning is performed on a 3D uniform lattice of voxels, Z, with the neighborhood of a constituting point defined by (m, n) to determine the medial axis $F \in Z$. The neighborhood definition is needed to deploy the thinning algorithm and locally delete voxels until the unique F (thin skeleton) is determined.

In the final step, the subset F from Z is converted into a spatial graph. This is an important step, as the discrete set of points is now formally converted into a set of edges with connectivity matrix denoting the topology of the skeleton. Formally, the graph is an ordered pair $G = (V, E)$ comprising a set V of vertices, nodes or points together with a set E of edges, which are 2-element subsets of V. In the simplest case, the edge is a straight line. In the most complex case, the shape of the edge is described by a spline or curved surface. In general, the graph is a data structure that has several advantages important for this work. First of all, it provides a compact representation of microstructural topology. By converting microstructure into the graph, classic algorithms from graph theory can be applied to quantify various topological features, such as connectivity. Finally, in the context

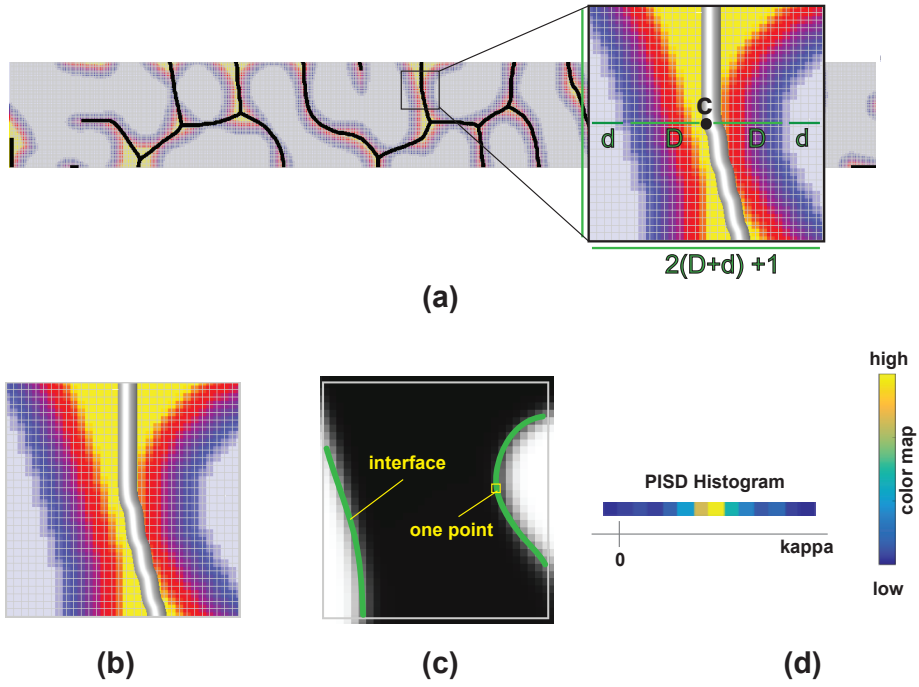

Figure 3: Protocol of patch extraction: Panel (a) shows three overlaid views of the 2D morphology (distance field, morphology pixels, and the skeleton. The zoomed-in view shows an example of a patch. C represents the patch center which always lies on the skeleton (or close to the skeleton). The distance field value is determined at C. The patch size is then a cube with size 2(D+d) pixels. Where d is a parameter selected by the user and 1 is the extra pixel at the center. In this example, D = 10 pixels and d = 5 pixels. Panels (b) and (c) represent the extraction of the interface and curvature extraction. Panel (d) represents the PISD histogram for one patch.

of this work, the graph is a preferred data structure as it guides the path extraction from the morphology.

Extracting patches and associated sizes

In the second step of the methodology, we identify a meaningful local region that we call patches (see Fig. 3). A patch is a local region inside the morphology that captures various aspects of the microstructure. This is an important step of the analysis as it introduces meso-scale into the microstructure representation. It allows partitioning the microstructure into building blocks facilitating the hierarchical quantification.

The choice of patch size is the most important aspect of patch extraction. In particular, it should reflect the mesoscale and enable statistical analysis. For example, too small patches capture very local features potentially missing key features. In other words, each patch would be indistinguishable defying any structure-property analysis. Too large patches, on the other hand, would lead to a very similar outcome as each patch would capture unique aspects of the microstructure making any statistical analysis infeasible. We additionally put the following constraints:

(1) The patch needs to include two or more corresponding interface fragments.

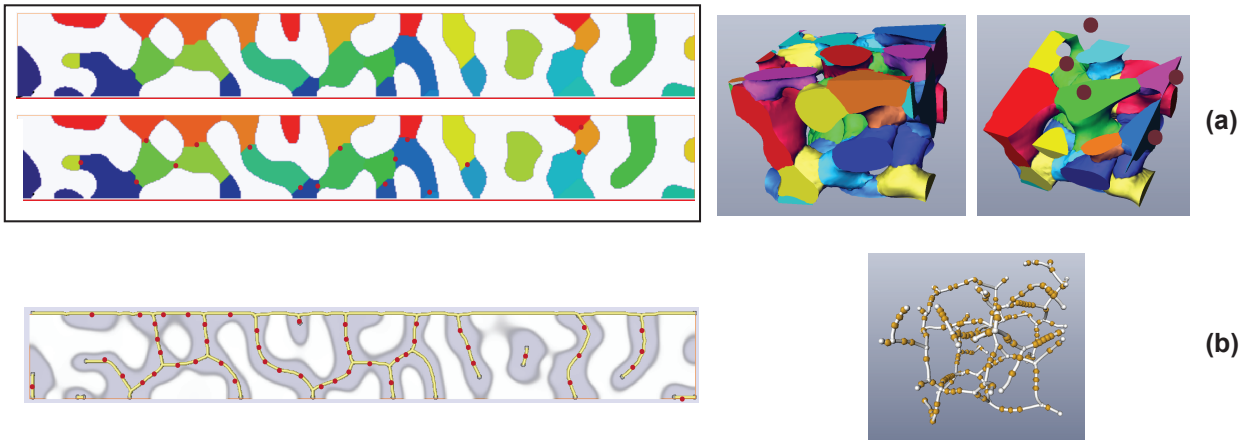

Figure 4: Two strategies for patch center selection, where the circles show the patch centers both in 2D and 3D. Panel (a) shows the choice of the patch centers guided by segmentation of the 2D morphology (upper row). In this strategy, we place the patch at the intersection between every two segments. This helps when the hour-glass shapes need to be identified. (b) Uniform distribution of the centers, on the backbone. The patches, in this case, are placed based on the length of the backbone as well as the patch sizes. This strategy is used when it is required to extract all curvatures and not hourglass shapes only. The 3D image to the right shows a sample of some patches with different sizes and centers.

(2) Each interface fragment captured within the patch needs to be large enough to define meaningful curvature while maintaining the locality of the patch.

(3) To avoid redundancy, the neighboring patches should not overlap.

To address the above requirements, we extract patches along the backbone of the morphology. To define the patch we need to choose the center. Since the backbone by definition is the medial axis of the structure, the patch center can be easily identified by retrieving one point from the skeleton. More importantly, any point chosen from the skeleton automatically satisfies the first constraint. Once path centers are chosen, the size of the patch needs to be decided. Here, we use the distance map determined in the skeletonization step (D). Accordingly, given a patch center C_i, the corresponding distance D_i from distance field is retrieved. Essentially, the distance D_i informs on the distance to the nearest interface as shown in Fig. 3(a). It is used to guide the patch size (constraint 2), where the final size S is chosen - as shown in Fig. 3(b) according to equation :

$$S = 2(D + d) \tag{2}$$

where d is the off-set chosen arbitrarily (constraint 3). The patch is either square or cubical with size S in 2D and 3D, respectively. The above protocol guarantees that patch extraction is adapted to the local features of the morphology. In particular, partitioning of morphologies with complex underlying topology will result in smaller patches, while coarse morphologies will lead to fewer patches of a larger size.

Finally, to guide the selection of the patch center, in the process of patch extraction input, morphology is decomposed into a set of patches along with the domain size. Two strategies can be employed:

1. **Topology-guided patch center distribution** For each backbone edge e from skeletal graph G, we compute the edge length l_e. Next, we place a patch center in the midpoint of that edge. From distance map D, we retrieve the distance d_e for the path center. If $d_e < l_e$, we add additional two patch centers on the backbone such that the edge is divided into three equal parts. The process is repeated until the condition is satisfied. The results are demonstrated in Figure 4(b). This strategy aims at uniform coverage of the backbone topology.
2. **Domain size-guided patch center distribution** For each backbone edge e from skeletal graph G, we extract an array of distances from map D. The array corresponds to all points from F constituting an edge e. Next, we place a patch center at the point where corresponding distance changes significantly along the edge. Effectively, the center of the patches is placed at the intersection of the regions as shown in Figure 4(a). We achieve this by applying a Watershed algorithm [21] on the distance map along with persistence-based [22] merging step. Example results are depicted in Figure 4, where color coding reflects regions of different sizes. In essence, this strategy is guided by local domain size and aims at extracting patches of similar size separated by bottlenecks.

Regardless of the strategy chosen, it is worth noting that the size of local features can be simultaneously extracted.

Patch Interface Shape Distribution (PISD) computation

Finally, once the patches are determined, we proceed to quantifying their shapes as follows. For each patch, we reconstruct the interface fragments as shown in Figure 3(b), (c). Next, for each point at the reconstructed surface, we calculate the principal curvatures (κ_1, κ_2). We aggregate the curvatures information in the form of distribution through Patch Interface Shape Distribution (PISD) [23]. PISD is defined by the probability density that a randomly chosen point on the patch surface will have a value between κ_1 and $\kappa_1+\delta\kappa_1$ and κ_2 and $\kappa_2+\delta\kappa_2$. This is computed as follows:

$$PISD(\kappa_1, \kappa_2) = A(\kappa_1, \kappa_2)/\delta\kappa_1\delta\kappa_2 A_I, \tag{3}$$

where $A(\kappa_1, \kappa_2)$ is the sum of the areas of the triangles in the interface mesh that has principal values of (κ_1, κ_2), A_I is the sum of the areas of all the triangles that fall on the patch interface surface. To get a meaningful comparison among the patches that have different sizes, we normalize the principal curvature. In particular, for each patch, we divide κ_1 and κ_2 by the surface-volume ratio $S_V = A_I/V$, where V is the volume of the one phase. An example histogram is depicted in Fig. 3(d). In Figure 5 (a), two patches with the corresponding PISD are depicted. We have chosen these shapes to demonstrate that PISD has capabilities to differentiate between significantly different shapes. In both cases, the interface is color-coded using Gaussian curvature. Three additional shapes are depicted in Figure 5 (b), namely sphere, and cylinder.

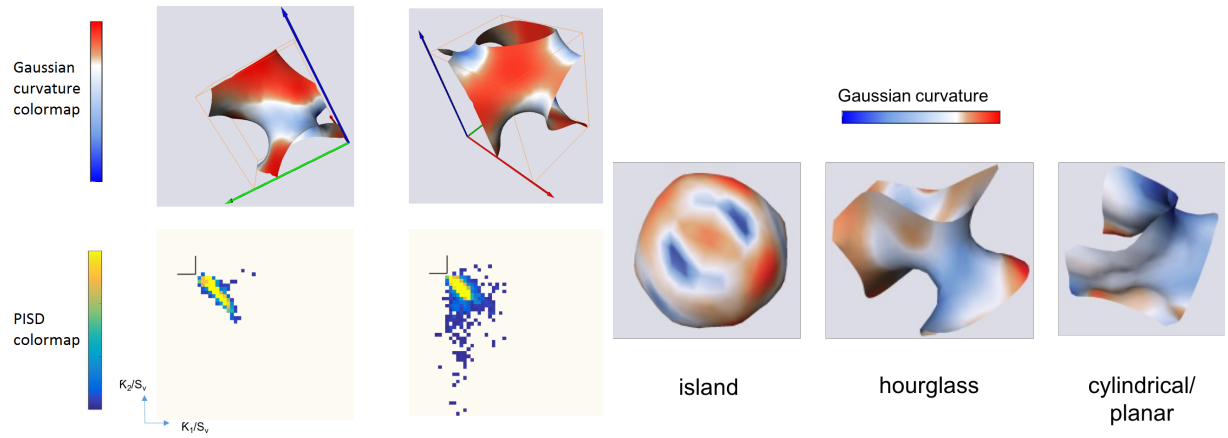

Figure 5: An illustration of PISD for different 3D patch shapes: the 3D patches are color-coded by Gaussian curvature to illustrate curvature distribution in 3D.

3. Technical details

Results generated for this paper leveraged a myriad of software. We used Amira to build our basic visualization system that has been adapted by implementing specialized plugins. We also used MATLAB and D3.js K-medoids clustering plugin to generate cluster view. Preprocessing and visualization were executed on Intel Xeon CPU E5-2698 v3 @ 2.30GHz with two processors with 128 GB RAM.

4. Results

To showcase the capability of our framework, we perform three step quantification of the representative microstructures that follow spinodal decomposition [24, 25]. Spinodal decomposition is a microstructure evolution mechanism. It is crucial for many applications including fabrication of organic solar cells [24] that has been the main science driver for this work. In particular, the kinetics of spinodal decomposition is directly linked with the fabrication process and controls the properties of these devices. Hence, understanding how morphological features evolve in time is of importance for the design of the fabrication process [24]. The methodology presented in this paper is leveraged to perform characterization and enable quantitative understanding of morphology evolution. The results section is organized into four sections, and we begin by providing details on the data generation process and then discussing three-step quantification of morphological samples.

4.1. Data generation

We study microstructure evolution of a binary system following spinodal decomposition [25]. This is an interesting mechanism characterized by a rich and complex collection of interacting phenomena. In our example, the binary mixture of two polymers initially separates into phases very rapidly (phase-separation), followed by slow, and sporadic coarsening events. We use the physics-based framework to generate large data sets of morphologies [26, 25]. The framework is based on a governing equation called the Cahn-Hilliard

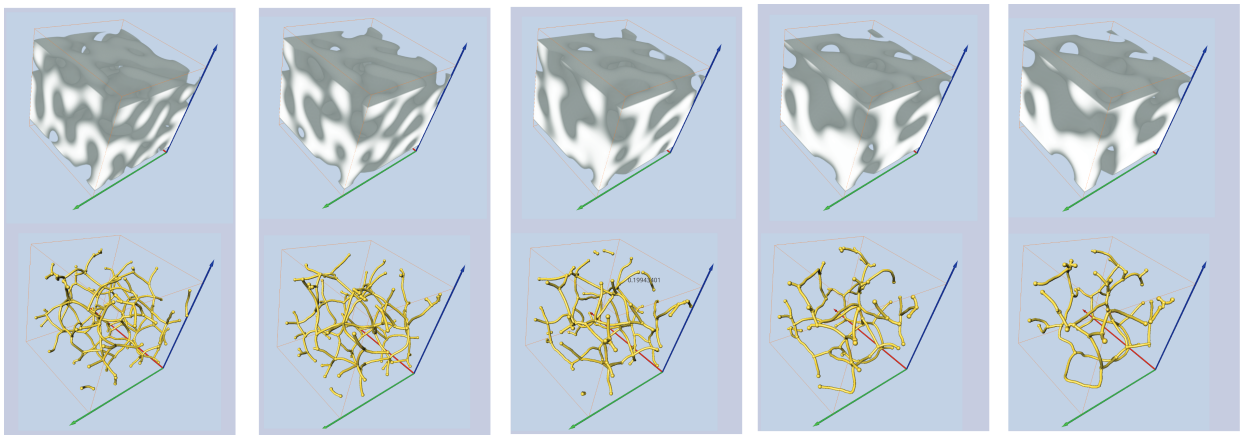

Figure 6: The time series of microstructure along with the backbone extraction and statistics (table).

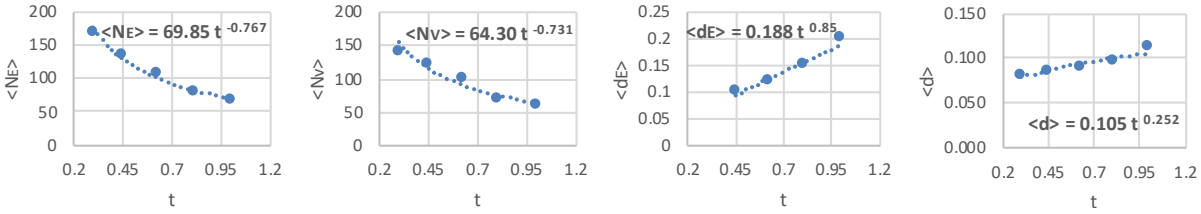

Figure 7: Rate of change for selected features for spinodal decomposition microstructures: number of edges $< N_E >= 69.85t^{-0.77}$, number of vertices $< N_V >= 64.3t^{-0.73}$, edge length $< d_E >= 0.188t^{0.85}$, and patch size $< d >= 0.105t^{0.25}$.

equation [27] that encompasses the kinetics of both phase separation and coarsening:

$$\frac{\partial \phi}{\partial t} = \nabla \cdot \left(M \frac{\partial f}{\partial \phi} - Cn^2 \nabla^2 \phi \right) \tag{4}$$

where $\phi(x,t)$ is the volume fraction of the polymer, which evolves in time and space, M is the mobility, Cn is the Cahn number and f is the free energy. By solving this equation, we predict the spatiotemporal morphology evolution, in the form of $\phi(x,t)$, for a two-component system (two polymers). Example time series evolution of the binary system is illustrated in Figure 6, where two components are mixed with a 1:1 ratio. We selected a dataset of 5 morphologies representative for few stages of the underlying process. We quantify five three dimensional morphologies corresponding to selected times: t=0.2, 0.4, 0.8 and 1.0, respectively. In each case, the size of each morphology is 50×50×50 voxels. White regions correspond to a phase that is rich in one polymer, while gray regions correspond to a phase rich in another polymer.

4.2. Topology quantification

For each microstructure in the dataset, we compute the backbone following the procedure detailed in section 2.1. Figure 6 depicts the backbones along with the corresponding morphologies and extracted statistics. In particular, the top panels of this figure illustrate the

phase distribution within the sample volume, while bottom panels depict the corresponding backbones for five morphologies. It should be noted that topology can be determined by both phases (black and white), here we only show backbones computed for the semi-transparent grey phase (top panels).

The first time snapshot corresponds to the morphology representative for the phase separation process. At this stage, the backbone consists of 167 edges exposing the richness of initial morphology (t=0.1) with 83 branching vertices. As time progresses, and morphology coarsens, the number of edges gradually decreases to 67 edges for the last studied snapshot (t=1.0). This is not surprising, as in this evolution stage (between t_1 and t_5) morphology exhibits clear coarsening process. During coarsening, the interfacial energy is dissipated. It is accompanied by (i) a decrease of the interface area between phases and (ii) an increase in the domain size. To quantify the rate of morphological changes, we determine the corresponding coarsening laws. In general, the coarsening laws have been mostly centered around effects of domain sizes, e.g., $< d > \sim t^{1/3}$ where d is the domain size [28, 29]. Recently, coarsening laws have been discussed in the context of topology [30]. The protocol developed in this paper expands this discussion into another set of morphological features. We select few features of backbone and trace the rate of change for the dataset. The corresponding results are depicted in Figure 6.

We selected four topological descriptors for investigation: the total number of edges,the total number of vertices, and the average edge length and the average patch size. This figure also includes the associated power laws for each descriptor. The analysis of the power laws reveals the diverse range of scaling exponent. For example, the average edge length, $< d_E >$, increases with time following a power law with the exponent of 0.85 ($< d_E >= 0.19t^{0.85}$). This is 2.5 times higher than the scaling exponent typical for the domain sizes [28, 29].

4.3. Size quantification

Next, we move to the size quantification. In our framework, two types of domain sizes can be extracted: main backbone edge length and the patch size. Moreover, as a part of the skeletonization algorithm, we compute the distance field from the domain boundary. We also looked into the rate of change of domain size for morphology evolution. Figure 7 shows the average patch size increasing with time ($< d >= 0.105t^{0.25}$). This is similar trend to the edge length trend discussed in the previous subsection. However, this time, the determined exponent is much smaller, namely 0.25. It is interesting to observe that although both descriptors capture domain size feature, they follow different scaling laws. The distinction between two types of size features becomes more important for the highly fibrous networks [31], and motivates quantifying the myriad of size-related features.

4.4. Shape classification

The final step of morphology quantification involves the shape classification. Here, we focus on the local shape extraction as opposite to shape quantification averaged over the entire sample [30]. Similar to size quantification, we begin with partitioning morphologies into patches. We leverage the skeletons computed in the previous step (Figure 7). As an outcome 1234 patches are generated using the domain size-guided strategy from subsection 2.1 and

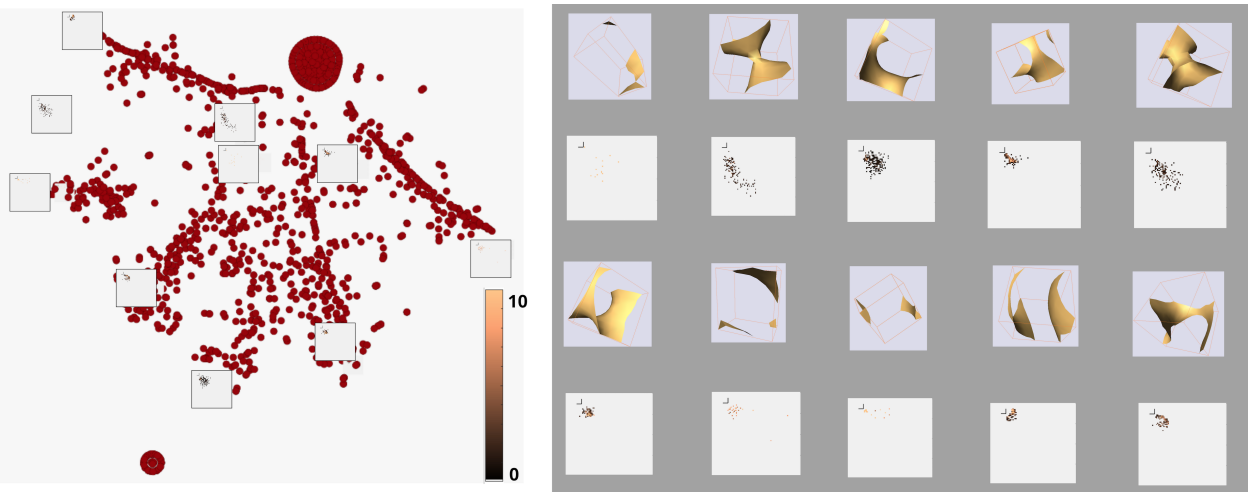

Figure 8: The figure illustrates the patch PISD views used for exploring the given data set. Panel (a) illustrates the cluster view produced by the t-SNE algorithm. This view gives an overview of all the patches of the dataset. Panel (b) illustrates the medoid patches generated by the k-medoid algorithm.

Figure 3. For each patch, we compute a PISD (30X30 resolution of interface reconstructed) and executed Principal Component Analysis (PCA) to reduce the representation of PISD into a manageable feature vector. Next, we execute the t-SNE algorithm [32] to view shape distribution of all patches while preserving the similarities between them. We use the first ten components of the PCA to execute t-SNE. The view generated by the t-SNE is shown in Figure 8. This algorithm gives each data point, in this case each patch, a location in a two-dimensional map. The outcome map provides quick insight into the dataset and can be used for clustering and classification.

To demonstrate the utility of this step, we chose cylindrical patch shape and extracted all patches of this type. To achieve it, we first identify PISDs characteristic for cylindrical shapes. Next, we performed k-medoids clustering algorithm [33] on PCA-based feature vectors. We found that our data set nicely into ten clear clusters. Finally, we extract the medoid that represents the cylindrical cluster along with the patches. The corresponding cylindrical patches are shown in Figure 9 (a) along with selected PISD. Inspection of these patches confirms that they are cylindrical, although none of the patches is a perfect cylinder. Finally, the extracted patches are mapped back to the input morphologies. We computed the total number of cylindrical patch per microstructure. The distribution of the cylindrical patches is represented in Figure 9 (b). Our analysis reveals that the number of cylindrical patches per morphology gradually decreases with time, while patch fraction remains constant with time.

5. Conclusion

In this work, we presented the methodology to extract morphology descriptors ranging from topology to size-related descriptors. The unique aspect of this work lies in the systematic protocol to fine tune various features, rather than focusing on one well-defined feature.

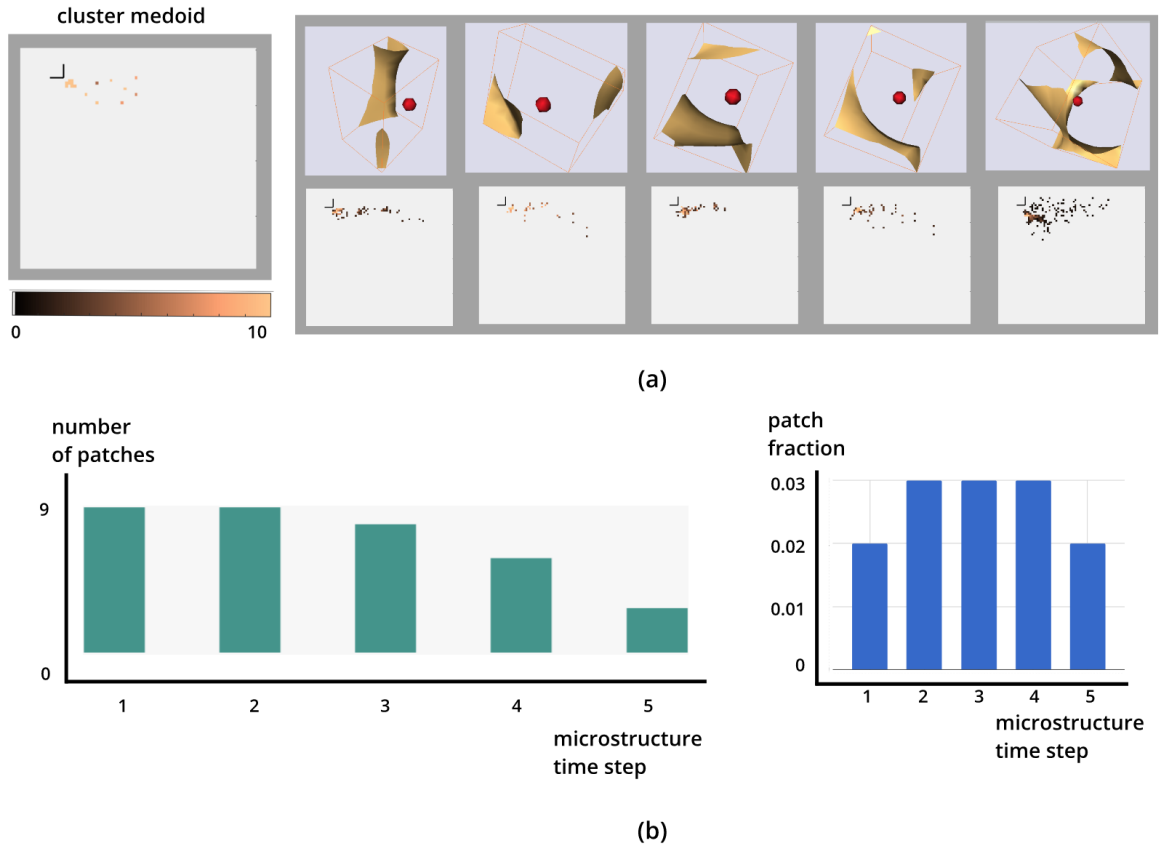

Figure 9: The figure illustrates the visual views used to explore one cluster of interest. The cluster includes the patches that have high distribution along the x-axis which denotes the high distribution of cylindrical regions. The left view shows the patches that belong to the cluster. The histogram shows the distribution of these patches at each microstructure. The icons show 3D examples of the patches that belong to this cluster.

For example, we extract two types of domain sizes, namely the averaged edge length, and the patch size. Using this methodology, we determined the scaling laws for the rate of change for selected features during spinodal decomposition. Interestingly, the rate laws are sensitive to the type of size considered. Here, we only showcase the utility of the feature extraction and their utility to establish rate laws, and we defer detailed discussion on the coarsening laws to the separate paper. The methodology is extensible to other types of the microstructure.

The work presented in this paper is the first step towards more extensive feature extraction from heterogeneous microstructural samples. This methodology opens novel avenues to study coarsening laws in materials science. Finally, this methodology lays the foundation for microstructure property-based machine learning, where salient feature selection is derived from the comprehensive library of diverse descriptors.

Data availability

The datasets generated and analyzed during the current study are available from the corresponding authors on reasonable request.

6. Acknowledgments

This work was supported in part by King Abdullah University of Science and Technology (KAUST) and National Science Foundation (1906344). OW acknowledges the support provided by the Center for Computational Research at the University at Buffalo.

[1] Krishna Rajan, Changwon Suh, Arun Rajagopalan, and Xiang Li. Quantitative structure-activity relationships (qsars) for materials science. *MRS Online Proceedings Library Archive*, 700, 2001.

[2] Tu Le, V Chandana Epa, Frank R Burden, and David A Winkler. Quantitative structure–property relationship modeling of diverse materials properties. *Chemical reviews*, 112(5):2889–2919, 2012.

[3] Francesco Brun, Lucia Mancini, Parnian Kasae, Stefano Favretto, Diego Dreossi, and Giuliana Tromba. Pore3d: A software library for quantitative analysis of porous media. *Nuclear Instruments and Methods in Physics Research Section A: Accelerators, Spectrometers, Detectors and Associated Equipment*, 615(3):326–332, 2010.

[4] RW Armstrong, I Codd, RM Douthwaite, and NJ Petch. The plastic deformation of polycrystalline aggregates. *Philosophical Magazine*, 7(73):45–58, 1962.

[5] Yuan Li, Andy J Bushby, and David J Dunstan. The hall–petch effect as a manifestation of the general size effect. In *Proc. R. Soc. A*, volume 472.2190, page 20150890. The Royal Society, 2016.

[6] A. Carpinteri and N. Pugno. Are scaling laws on strength of solids related to mechanics or to geometry? *Nature Materials*, 4(6):421–423, 2005.

[7] K.R. Mangipudi, E. Epler, and C.A. Volkert. Topology-dependent scaling laws for the stiffness and strength of nanoporous gold. *Acta Materialia*, 119:115–122, 2016.

[8] Sathish Kottravel, Riccardo Volpi, Mathieu Linares, Timo Ropinski, and Ingrid Hotz. Visual analysis of stochastic trajectory ensembles in organic solar cell design. In *Informatics*, volume 4, page 25. Multidisciplinary Digital Publishing Institute, 2017.

[9] Amal Aboulhassan, Daniel Baum, Olga Wodo, Baskar Ganapathysubramanian, Aram Amassian, and Markus Hadwiger. A novel framework for visual detection and exploration of performance bottlenecks in organic photovoltaic solar cell materials. In *Computer Graphics Forum*, volume 34, pages 401–410. Wiley Online Library, 2015.

[10] Amal Aboulhassan, Ronell Sicat, Daniel Baum, Olga Wodo, and Markus Hadwiger. Comparative visual analysis of structure-performance relations in complex bulk-heterojunction morphologies. In *Computer Graphics Forum*, volume 36, pages 329–339. Wiley Online Library, 2017.

[11] C.-L. Park, J.W. Gibbs, P.W. Voorhees, and K. Thornton. Coarsening of complex microstructures following spinodal decomposition. *Acta Materialia*, 132:13 – 24, 2017.

[12] Krishna Rajan. Phase transformations in a wrought co-cr-mo-c alloy. *Metallurgical Transactions A*, 13(7):1161–1166, 1982.

[13] Olga Wodo, John Roehling, Adam Moule, and Baskar Ganapathsubramanian. Quantifying organic solar cell morphology: A computational study of three-dimensional maps. *Energy and Environmental Science*, 6:3060–3070, 2013.

[14] Long-Qing Chen. Phase-field models for microstructure evolution. *Annual review of materials research*, 32(1):113–140, 2002.

[15] Cheng-Kuang Lee, Olga Wodo, Baskar Ganapathysubramanian, and Chun-Wei Pao. Electrode materials, thermal annealing sequences, and lateral/vertical phase separation of polymer solar cells from multiscale molecular simulations. *ACS applied materials & interfaces*, 6(23):20612–20624, 2014.

[16] S Samudrala, O Wodo, SK Suram, S Broderick, K Rajan, and B Ganapathysubramanian. A graph-theoretic approach for characterization of precipitates from atom probe tomography data. *Computational Materials Science*, 77:335–342, 2013.

[17] Chris Pudney. Distance-ordered Homotopic Thinning: A Skeletonization Algorithm for 3D Digital Images. *Computer Vision and Image Understanding*, 72(3):404–413, 1998.

[18] Gunilla Borgefors. Distance transformations in digital images. *Computer vision, graphics, and image processing*, 34(3):344–371, 1986.

[19] Jonathan W Brandt and V Ralph Algazi. Continuous skeleton computation by voronoi diagram. *CVGIP: Image understanding*, 55(3):329–338, 1992.

[20] Jayanta Mukherjee, BN Chatterji, and Partha Pratim Das. Thinning of 3-d images using the safe point thinning algorithm (spta). *Pattern Recognition Letters*, 10(3):167–173, 1989.

[21] Michel Couprie and Gilles Bertrand. Topological gray-scale watershed transformation. *Proc. SPIE*, 3168(6):136–146, 1997.

[22] Herbert Edelsbrunner, David Letscher, and Afra Zomorodian. Topological persistence and simplification. *Discrete and Computational Geometry*, 28(4):511–533, 2002.

[23] Yu-chen Karen Chen, Yong S Chu, JaeMock Yi, Ian McNulty, Qun Shen, Peter W Voorhees, and David C Dunand. Morphological and topological analysis of coarsened nanoporous gold by x-ray nanotomography. *Applied Physics Letters*, 96(4):043122, 2010.

[24] O. Wodo and B. Ganapathysubramanian. Modeling morphology evolution during solvent-based fabrication of organic solar cells. *Computational Materials Science*, 55, April 2012.

[25] Olga Wodo and Baskar Ganapathysubramanian. Computationally efficient solution to the cahn–hilliard equation: Adaptive implicit time schemes, mesh sensitivity analysis and the 3d isoperimetric problem. *Journal of Computational Physics*, 230(15):6037–6060, 2011.

[26] Olga Wodo, Srikanta Tirthapura, Sumit Chaudhary, and Baskar Ganapathysubramanian. Computational characterization of bulk heterojunction nanomorphology. *Journal of Applied Physics*, 112(6), 2012.

[27] John W Cahn and John E Hilliard. Free energy of a nonuniform system. i. interfacial free energy. *The Journal of chemical physics*, 28(2):258–267, 1958.

[28] W Ruland. Small-angle scattering of two-phase systems: determination and significance of systematic deviations from porod's law. *Journal of Applied Crystallography*, 4(1):70–73, 1971.

[29] Georg Krausch, Edward J Kramer, Frank S Bates, JF Marko, G Brown, and A Chakrabarti. Surface-induced asymmetries during spinodal decomposition in off-critical polymer mixtures. *Macromolecules*, 27(23):6768–6776, 1994.

[30] Yongwoo Kwon, K Thornton, and PW Voorhees. Morphology and topology in coarsening of domains via non-conserved and conserved dynamics. *Philosophical Magazine*, 90(1-4):317–335, 2010.

[31] Muhammad Haneef, Luca Ceseracciu, Claudio Canale, Ilker S Bayer, Jose A Heredia-Guerrero, and Athanassia Athanassiou. Advanced materials from fungal mycelium: fabrication and tuning of physical properties. *Scientific reports*, 7:41292, 2017.

[32] Laurens van der Maaten and Geoffrey Hinton. Visualizing data using t-sne. *Journal of machine learning research*, 9(Nov):2579–2605, 2008.

[33] Leonard Kaufman and Peter J Rousseeuw. *Finding groups in data: an introduction to cluster analysis*, volume 344. John Wiley & Sons, 2009.